

Article

Comprehensive Comparisons of State-of-the-Art Gridded Precipitation Estimates for Hydrological Applications over Southern China

Zhen Gao ^{1,2,3,4}, Bensheng Huang ^{2,3,4}, Ziqiang Ma ⁵, Xiaohong Chen ^{1,*} , Jing Qiu ^{2,3,4} and Da Liu ^{2,3,4}

- ¹ Center for Water Resources and Environment Research, Sun Yat-sen University, Guangzhou 510275, China; gaozhen3@mail.sysu.edu.cn
 - ² Guangdong Research Institute of Water Resources and Hydropower, Guangzhou 510610, China; gdsky_hbs@gd.gov.cn (B.H.); gdsky_ghzx@gd.gov.cn (J.Q.); gdsky_szys@gd.gov.cn (D.L.)
 - ³ Guangdong-Hongkong-Macao Greater Bay Area Water Security Engineering Technology Research Center, Guangzhou 510610, China
 - ⁴ Guangdong Provincial Key Laboratory of Water Quality Improvement and Ecological Restoration for Watersheds, Guangzhou 510610, China
 - ⁵ Institute of Remote Sensing and Geographical Information Systems, School of Earth and Space Sciences, Peking University, Beijing 100871, China; ziqma@pku.edu.cn
- * Correspondence: eescxh@mail.sysu.edu.cn; Tel.: +86-135-0305-3520

Received: 23 October 2020; Accepted: 28 November 2020; Published: 6 December 2020



Abstract: Satellite-based precipitation estimates with high quality and spatial-temporal resolutions play a vital role in forcing global or regional meteorological, hydrological, and agricultural models, which are especially useful over large poorly gauged regions. In this study, we apply various statistical indicators to comprehensively analyze the quality and compare the performance of five newly released satellite and reanalysis precipitation products against China Merged Precipitation Analysis (CMPA) rain gauge data, respectively, with $0.1^\circ \times 0.1^\circ$ spatial resolution and two temporal scales (daily and hourly) over southern China from June to August in 2019. These include Precipitation Estimates from Remotely Sensed Information using Artificial Neural Networks Cloud Classification System (PERSIANN-CCS), European Center for Medium-Range Weather Forecasts Reanalysis v5 (ERA5-Land), Fengyun-4 (FY-4A), Global Satellite Mapping of Precipitation (GSMaP), and Integrated Multi-satellitE Retrievals for Global Precipitation Measurement (IMERG). Results indicate that: (1) all five products overestimate the accumulated rainfall in the summer, with FY-4A being the most severe; additionally, FY-4A cannot capture the spatial and temporal distribution characteristics of precipitation over southern China. (2) IMERG and GSMaP perform better than the other three datasets at both daily and hourly scales; IMERG correlates slightly better than GSMaP against CMPA data, while it performs worse than GSMaP in terms of probability of detection (POD). (3) ERA5-Land performs better than PERSIANN-CCS and FY-4A at daily scale but shows the worst correlation coefficient (CC), false alarm ratio (FAR), and equitable threat score (ETS) of all precipitation products at hourly scale. (4) The rankings of overall performance on precipitation estimations for this region are IMERG, GSMaP, ERA5-Land, PERSIANN-CCS, and FY-4A at daily scale; and IMERG, GSMaP, PERSIANN-CCS, FY-4A, and ERA5-Land at hourly scale. These findings will provide valuable feedback for improving the current satellite-based precipitation retrieval algorithms and also provide preliminary references for flood forecasting and natural disaster early warning.

Keywords: satellite precipitation; reanalysis precipitation; error analysis; FY-4A; southern China

1. Introduction

Precipitation is among the most important meteorological variables in global climate models and terrestrial hydrological cycles [1,2]. In recent decades, global warming-induced extreme climatic changes have increased the frequency of heavy rainfalls brought by typhoons in the south coast regions of China, which will cause geological disasters, such as landslides, urban floods, soil erosion, and severe storms [3]. Thus, accurate precipitation inputs with high spatial and temporal resolutions are crucial for reliable weather forecasting, hydrologic modeling, and agricultural studies [4]. Traditionally, because of the inherently strong spatiotemporal heterogeneity in rainfall fields, techniques for making precipitation observations from ground-based rain gauge networks have been very limited or unavailable [5]. Hydrologic modeling and forecasting is a challenging task over regions where little or no data are available, particularly in remote basins with complex terrain and in developing countries [6]. Previous studies suggest that 60%–80% of the uncertainties of hydrologic modeling is influenced by the uncertainty of precipitation data during summer [7]. Though rain gauges, ground weather radars, and ocean-based buoys are more accurate at the point or local scales, they cannot observe the whole globe [8]. Compared to in situ precipitation measurements, satellite-based precipitation products have more advantages in terms of markedly increased spatial coverage with high resolutions, and their data is publicly available.

Measurements to estimate precipitation dynamics at global and regional scales can be traced back to 1997 when the Tropical Rainfall Measuring Mission (TRMM) was launched. A growing number of high spatiotemporal resolution satellite precipitation estimates have since been developed in succession, and several institutions and organizations using different satellite techniques and retrieval algorithms have provided their data publicly. For instance, TRMM Multi-satellite Precipitation Analysis (TMPA) [9], the final run version of Integrated Multi-satellitE Retrievals for Global Precipitation Measurement (IMERG) [10], the passive microwave (PMW)-based Climate Prediction Center (CPC) MORPHing technique (CMORPH) [11], Precipitation Estimates from Remotely Sensed Information using Artificial Neural Networks Cloud Classification System (PERSIANN-CCS) [12,13], the gauge-corrected version of Global Satellite Mapping of Precipitation (GSMaP) [14], Multi-Source Weighted-Ensemble Precipitation (MSWEP) [15], and Chinese Fengyun (FY) Quantitative Precipitation Estimation (QPE) and its improved version FY-4A [16]. Additionally, the fifth generation of the European Center for Medium-Range Weather Forecasts (ECMWF) reanalysis database (ERA5), could provide a more spatially and temporally homogeneous alternative to point-based observations [17]. Consequently, it is essential to comprehensively analyze satellite-based precipitation products from the perspective of time and region, which will effectively provide data users and algorithm developers with valuable guidance to understand their characteristics [18–20].

Over the past few decades, a large number of studies have been performed to examine the error structure and characteristics of satellite-based QPE products under different time and space scales for broad applications. Satellite-based QPE products have been widely applied in hydrology, meteorology, agriculture, and other research [21–27]. During the last three years, Tang et al. [8] evaluated IMERG at daily and hourly scales from 2000 to 2018 and compared it to nine satellite and reanalysis precipitation products in China. Yu et al. [18] evaluated CHIRPS, Global Precipitation Measurement (GPM) IMERG, and PERSIANN-CCS at daily scale in different seasons from 2015 to 2018 in different basins of China. Vizy and Cook [28] analyzed the relationship between the jet and boreal summer rainfall variability of TRMM, IMERG, CMORPH, ERA5, and MERRA2 from 2000 to 2017 in the jet exit region over South Sudan. Xu et al. [16] evaluated FY-2 and IMERG at $0.1^\circ \times 0.1^\circ$ resolution at hourly, daily, and monthly scales over mainland China in the summer of 2018. Zhang et al. [29] evaluated IMERG and GSMaP during the May 2017 Guangdong extreme rainfall event. Islam et al. [30] compared and evaluated IMERG with four other popular satellite precipitation products over the diverse climate zones of Australia against the daily gauge-based SILO dataset over a period of 5 years from October 2014 to September 2019. Zhou et al. [31] evaluated the performance of IMERG and GSMaP products over mainland China from 1 January 2015 to 31 December 2017, using daily precipitation data from

778 meteorological stations. However, only a few studies have evaluated the accuracy of FY-4A QPE or compared it with other widely used satellite-based precipitation products. Given the new capabilities, this study aimed to provide a comprehensive evaluation for the main current satellite and reanalysis precipitation products over southern China in 2019. Therefore, we selected the latest version of five satellite and reanalysis precipitation products (FY-4A, PERSIANN-CCS, GSMaP, IMERG, and ERA5-Land) at $0.1^\circ \times 0.1^\circ$ spatial resolution, both at hourly and daily scales, over the provinces of Guangxi and Guangdong in summer 2019.

The objectives of this study are twofold: (1) to evaluate and compare the five precipitation products, including FY-4A, PERSIANN-CCS, GSMaP, IMERG, and ERA5-Land, at hourly and daily scales using China Merged Precipitation Analysis (CMPA) in Guangxi and Guangdong provinces; (2) To analyze the potential error sources of the main current satellite-based precipitation products over southern China in the summer of 2019. New findings on the uncertainties of various precipitation products are demonstrated and discussed.

2. Materials and Methods

2.1. Study Region

The study region included the provinces of Guangxi and Guangdong in southern China, located within $104^\circ 28' - 117^\circ 19' E$ and $20^\circ 12' - 26^\circ 24' N$ (Figure 1). Together with the Guangxi region, Guangdong is clearly separated from the Yangtze River basin by the Nanling Mountains in the north. Guangdong has one of the longest coastlines of any Chinese province, fronting the South China Sea to the south (including connections to Hong Kong and Macau). This province is the most densely populated and economically developed region in China. It is $179,700 \text{ km}^2$, encompassing the flat Pearl River Delta (PRD) in a trumpet-shaped topography. The elevations range from 0 m on the coast to 1848 m in the north, and flat plains are scattered in the coastal region near the Leizhou Peninsula in the southwest and the PRD in the center. Climatically, this region is dominated by monsoon and tropical cyclones, with mean annual precipitation and temperature of $\sim 1777 \text{ mm}$ and $19\text{--}24^\circ \text{C}$, respectively. The rainfall regime shows a pronounced summer maximum, and more than 80% and 50% of annual precipitation occurs during the wet season (from April to September) and the summer (from June to August), respectively. Due to the combined effects of the complex terrain and the East Asian monsoon climate, typhoon-induced storm rain events and waterlogging frequently occur in Guangdong [32].

The Guangxi Zhuang Autonomous Region is located in the middle and upper reaches of the Pearl River, facing the Beibu Gulf on the South China Sea, and has a border with Vietnam to the southwest. As a whole, this province is like a large basin with the higher ground surrounding a lower center, and is very mountainous with a few plains. The elevations range from 0 m on the coast to 1972.3 m in the north, and the area is $237,600 \text{ km}^2$. The predominance of limestone gives many parts of Guangxi a spectacular type of landscape known as karst, in which pinnacles and spires, caves and caverns, sinkholes, and subterranean streams abound. Lying in low latitude areas and straddling the Tropic of Cancer, this region has a subtropical/tropical monsoon climate, with mean annual precipitation and temperature of $\sim 1695 \text{ mm}$ and $17.5\text{--}23.5^\circ \text{C}$, respectively. Together with Guangdong, approximately 80% of annual rain falls between April and September in Guangxi, and July is the warmest month. Drier areas are in the northwest, while the wetter areas are in the south and east. In the extreme south, rain bursts caused by typhoons (tropical cyclones) generally occur between July and September.

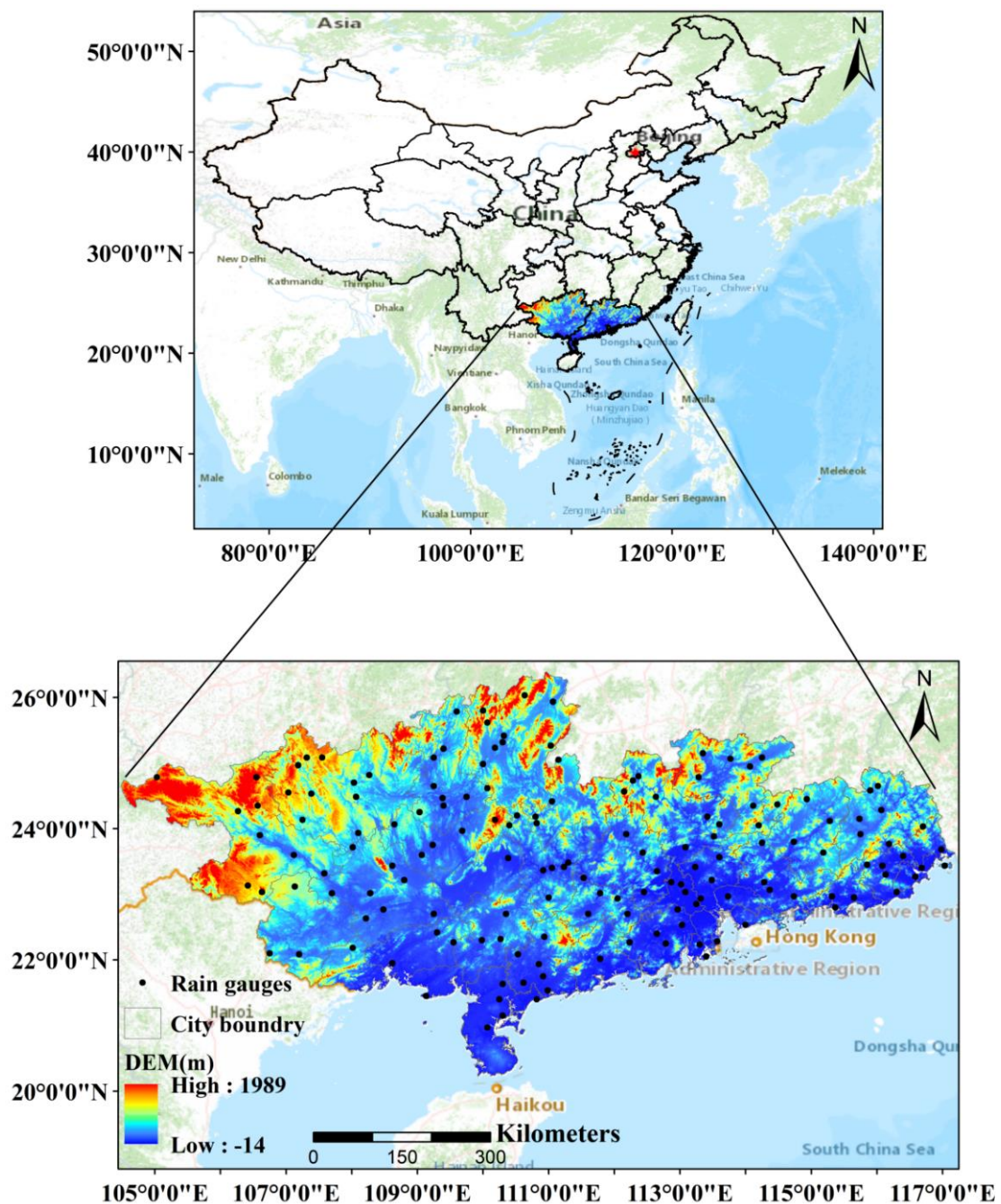


Figure 1. Spatial patterns of DEM over southern China, i.e., Guangdong and Guangxi province.

2.2. Datasets

2.2.1. CMPA

The China Merged Precipitation Analysis (CMPA, $0.1^\circ/\text{h}$) is generated using hourly rain gauge data from more than 30,000 automatic weather stations in China, combined with the CMORPH precipitation products, and is provided by the National Meteorological Information Center of the China Meteorological Administration [33]. Specifically, CMORPH products at fine spatial (8 km) and temporal (30 min) resolutions are resampled into $0.1^\circ/\text{h}$. The Optimal Interpolation (OI) method is adopted to estimate the areal precipitation distribution based on the gauge observations [34]. For grid boxes with gauges, the observed precipitation values are very reliable when more than one gauge is located in a grid. There are a total of 3652 grid pixels covering the Guangxi and Guangdong regions in

this study. As the hourly rain gauge datasets from 2163 national ground stations are collected from the National Meteorological Information Center (NMIC) of the CMA (<http://data.cma.cn>), the spatial distribution of 155 ground stations in southern China is shown in Figure 1.

2.2.2. Satellite and reanalysis precipitation products

Four satellite-based products and one reanalysis precipitation product are compared with basic information, and the references are summarized in Table 1. The Fengyun-4 Meteorological Satellite Series is the second generation of geostationary orbit meteorological satellite developed by China, upgraded from the previous FY-2 series. Currently, FY-4A is enabled with vertical atmospheric sounding and microwave detection capabilities to address 3D remote sensing at geostationary altitudes. As the first and the only satellite of the FY-4 series, FY-4A provides 32 quantitative satellite-based products, including Quantitative Precipitation Estimation. The fine spatial resolution (4 km) and temporal resolution (30 min) precipitation products used in this study can be downloaded from NSMC.

Table 1. Summary of the satellite and reanalysis datasets used in this study.

Dataset	Full Name of the Dataset	Resolution	Period	Latency	Reference
FY-4A	Fengyun 4A Quantitative Precipitation Estimation	4 km/0.5 h	2018–present	9 hours	[33]
PERSIANN-CCS	Precipitation Estimation from Remotely Sensed Information using Artificial Neural Networks Cloud Classification System	0.04°/0.5 h	2006–present	1 hour	[12]
ERA5-Land	European Center for Medium-Range Weather Forecasts Reanalysis v5	0.1°/1 h	1979–present	2 months	[35]
GSMaP	Global Satellite Mapping of Precipitation (Gauge) Integrated Multi-satellitE	0.1°/1 h	2000–present	3 days	[14]
IMERG	Retrievals for Global Precipitation Measurement Final	0.1°/1 h	2000–present	3.5 months	[10]

The PERSIANN is produced by NOAA using Artificial Neural Network (ANN) algorithm and is used to estimate rainfall rate with infrared brightness temperature data. PERSIANN-CCS applies the algorithm that extracts local and regional cloud features from infrared (10.7 mm) geostationary satellite imagery aiming to estimate finer scale (0.04° and 30 min) precipitation distribution. The PERSIANN-CCS and FY-4A were resampled to the 0.1° resolution and accumulated to the hourly scale to be consistent with CMPA datasets. The resampling method was linear interpolation for PERSIANN-CCS at the 0.04° resolution and FY-4A at the 4 km spatial resolution.

ERA5, the new climate reanalysis dataset from the European Center for Medium-Range Weather Forecasts (ECMWF), provides important data for understanding global precipitation [35]. Compared with previous precipitation products by the ECMWF, the most substantial upgrades of ERA5-Land are at the finer spatial and temporal resolution (0.1°/h). The comparison between reanalysis and satellite-based products could help illuminate their advantages and disadvantages so that they can be better applied and improved.

GSMaP products combine various available data from PMW and IR sensors, providing a global rainfall distribution map from the GPM mission to retrieve precipitation rates developed by JAXA with a high spatiotemporal resolution of 0.01°/h. The GSMaP (Gauge) product was gauge-calibrated based on the National Oceanic and Atmospheric Administration (NOAA) Climate Prediction Center (CPC) analysis of global daily precipitation.

IMERG focuses on intercalibrating, merging, and interpolating all satellite MW-based precipitation estimates, together with MW calibrated IR-based precipitation estimates, precipitation gauge analyses, and potentially other precipitation estimators at fine spatiotemporal scales for TRMM and GPM eras over the entire globe. The IMERG-Final dataset is a level 3 precipitation product of GPM, which was calibrated based on the Global Precipitation Climatology Center (GPCC) monthly gauge analysis. Because IMERG Final offers a fine temporal resolution of 30 min, the hourly data used in this study was obtained by averaging the two data files in the same hour.

2.3. Methodology

To evaluate the accuracy of mainstream satellite-based precipitation products against the real data and assess the detection capabilities in precipitation events of these satellite precipitation products, six widely used statistical metrics were applied in this study.

As shown in Table 2, three indices were adopted to evaluate the capability of precipitation products in the detection of precipitation events, namely, the probability of detection (POD), false alarm ratio (FAR), and equitable threat score (ETS). POD is usually used to represent the fraction of precipitation events correctly detected by the satellite among all actual precipitation events. FAR denotes the ratio of false alarms among all events detected by the satellite. ETS measures the skill of a forecast relative to chance and is less dependent on the relative occurrence of wet samples in the verification of precipitation forecasts. To discriminate between wet and dry samples, the thresholds of 0.1 mm/h were used for hourly samples.

Table 2. Equations and the best values of three contingency statistical indices.

Index	Equation ¹	Perfect Value
Probability of detection (POD)	$POD = \frac{H}{H+M}$	1
False alarm ratio (FAR)	$FAR = \frac{F}{H+F}$	0
Equitable threat score (ETS)	$ETS = \frac{H-(H+M)(H+F)/n}{H+M+F-(H+M)(H+F)/n}$	1

¹ Notation: H, observed rain correctly detected; M, observed rain not detected; F, rain detected but not observed; n, the total number of verification points.

The correlation coefficient (CC) describes the agreement between satellite precipitation data and real data with a value from 0 to 1. The relative bias (BIAS) and the root-mean-square error (RMSE) are widely used to quantitatively represent the error characteristics between the estimates and the real data. The equation and perfect values of these metrics are listed in Table 3.

Table 3. Equations and the best values of three statistical indices.

Statistic Index	Equation ¹	Perfect Value
Correlation coefficient (CC)	$CC = \sqrt{\frac{\sum_{i=1}^n (O_i - \bar{O})^2 (P_i - \bar{P})^2}{\sum_{i=1}^n (O_i - \bar{O})^2 \times \sum_{i=1}^n (P_i - \bar{P})^2}}$	1
Relative bias (BIAS)	$BIAS = \frac{\sum_{i=1}^n (P_i - O_i)}{\sum_{i=1}^n O_i} \times 100\%$	0
Root-mean-square error (RMSE)	$RMSE = \sqrt{\frac{1}{n} \sum_{i=1}^n (P_i - O_i)^2}$	0

¹ Notation: O_i , the amount of precipitation observed by real data; \bar{O} , the average true values, P_i , the estimated values of the satellite-based precipitation product; \bar{P} , the average estimated precipitation; n, the number of precipitation pairs of real data and the corresponding satellite-based estimates.

To demonstrate the temporal error characteristics of precipitation datasets, we used the Taylor diagram [36] to comprehensively evaluate the similarities between sets of variables or the reanalysis

and the reference. Taylor diagram integrates the CC, standard deviation (STD), and the centered root-mean-square difference (RMSD), which reflect how closely the various patterns in satellite-based precipitation products match those of ground observations. If the estimated pattern is closer to the reference data than other patterns in the diagram, it means that the accuracy of the estimates are better than others.

3. Results

3.1. Spatial Distributions of Accumulated Rainfall over Southern China in Summer 2019

The spatial distributions of accumulated rainfall for CMPA, PERSIANN-CCS, ERA5-Land, FY-4A, GSMaP, and IMERG products in the summer of 2019 over southern China are shown in Figure 2a–f, respectively. The precipitation in the southern coastal and northeast mountain areas of Guangxi province is relatively large, followed by Guangzhou, the capital city of Guangdong province (Figure 2a). Meanwhile, the spatial differentials of total rainfall estimated by PERSIANN-CCS, ERA5-Land, FY-4A, GSMaP, and IMERG products are shown in Figure 3a–e, respectively. Compared with CMPA, all five products indicate overestimates of precipitation to a certain extent in Guangxi, and FY-4A presents the most serious overestimation. PERSIANN-CCS obviously underestimates precipitation in the northeast mountain areas of Guangxi, obtaining only a small amount (<400 mm) (Figure 3a). ERA5-Land underestimates the southern coastal area of Guangxi province and the precipitation in the city of Guangzhou (Figure 3b). FY-4A significantly overestimates precipitation in the northeast and southwest of Guangdong province, while it underestimates precipitation in Guangzhou (Figure 3c). In terms of the spatial pattern and volume of precipitation, GSMaP is much more similar to those of CMPA over the whole region (Figure 3d), and IMERG also agrees well with CMPA (Figure 3e). Therefore, FY-4A and PERSIANN-CCS could not capture the spatial characteristics of precipitation over southern China in summer 2019.

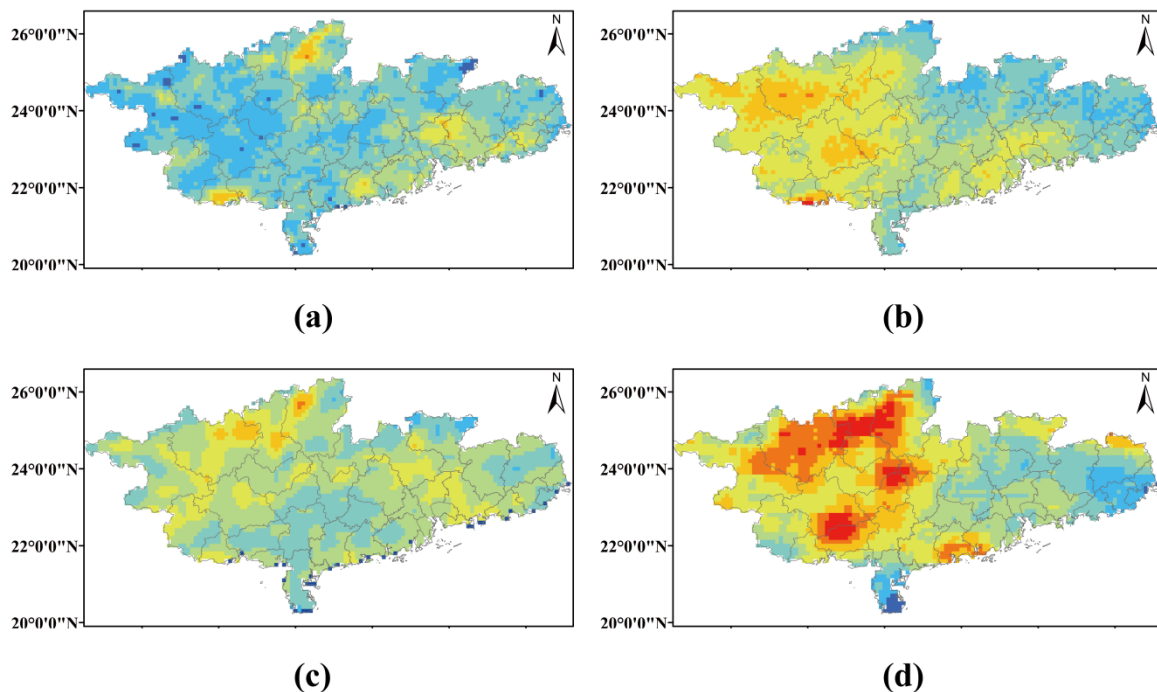


Figure 2. Cont.

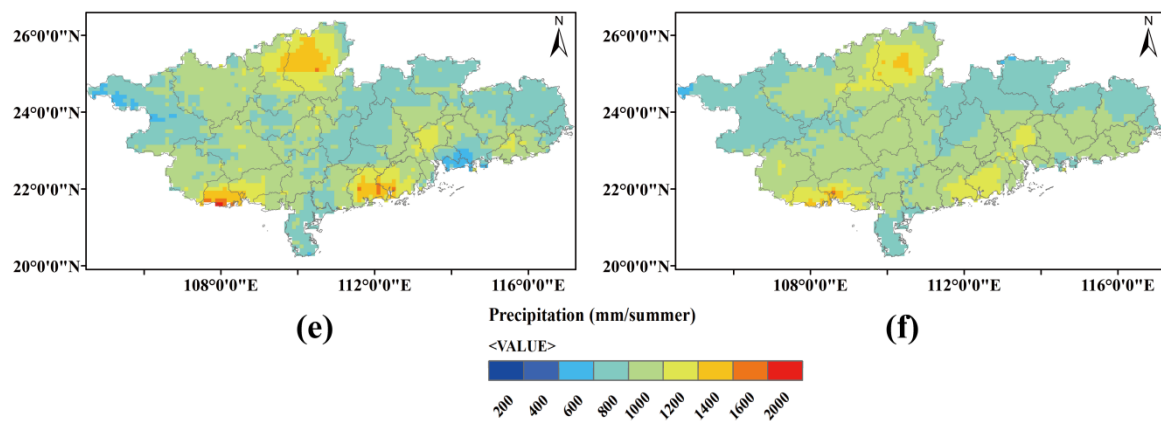


Figure 2. Spatial patterns of accumulated rainfall estimated by (a) China Merged Precipitation Analysis (CMPA), (b) Precipitation Estimates from Remotely Sensed Information using Artificial Neural Networks Cloud Classification System (PERSIANN-CCS), (c) European Center for Medium-Range Weather Forecasts Reanalysis v5 (ERA5-Land), (d) Fengyun-4 (FY-4A), (e) Global Satellite Mapping of Precipitation (GSMaP) (GSMaP), and (f) Multi-satellite Retrievals for Global Precipitation Measurement (IMERG) over southern China in summer 2019.

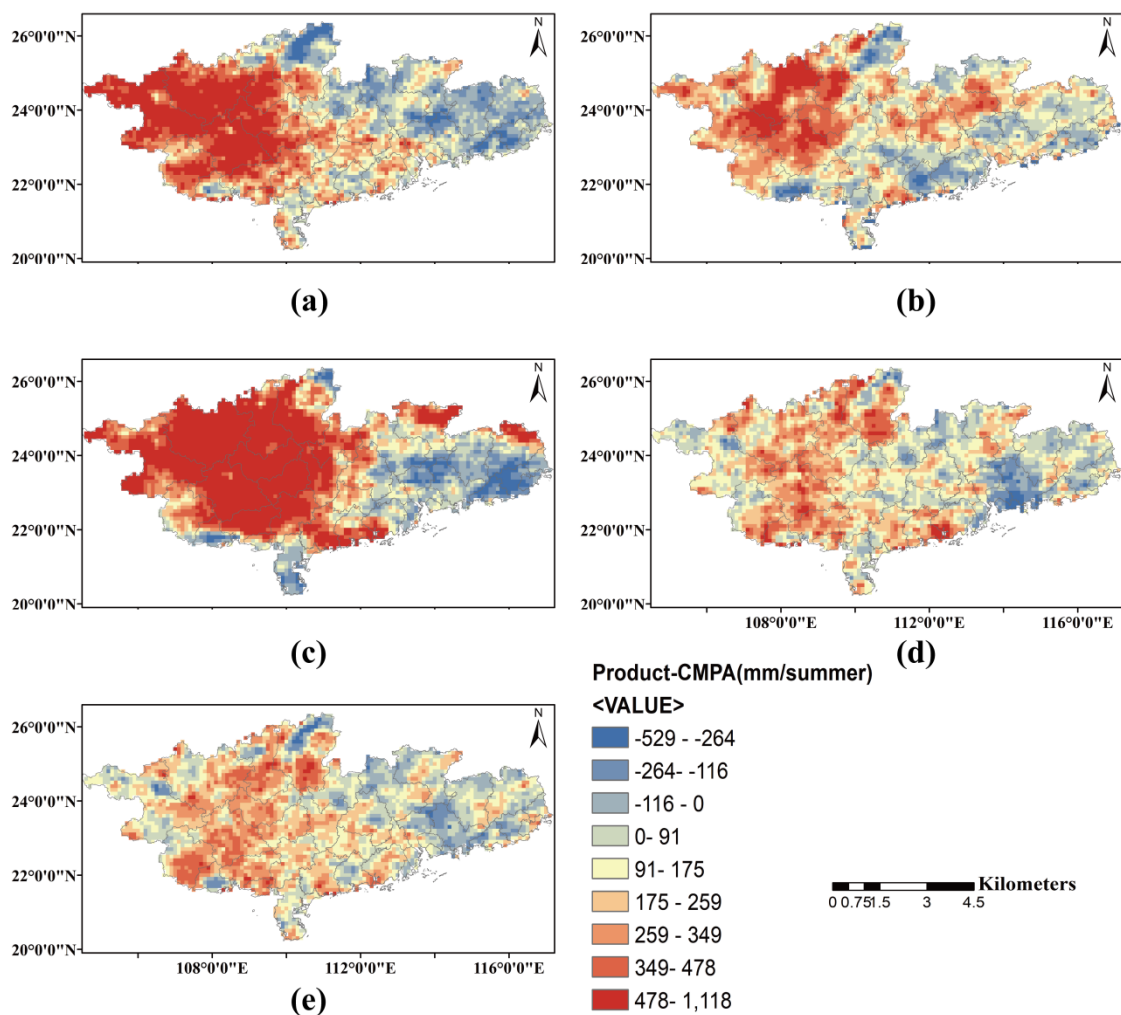


Figure 3. The spatial differentials of total rainfall estimated by (a) PERSIANN-CCS, (b) ERA5-Land, (c) FY-4A, (d) GSMaP, and (e) IMERG against CMPA over southern China in summer 2019.

3.2. Daily Scale Assessment of the Precipitation Products over Southern China from June to August

Precipitation time series variability significantly impacts hydrological processes over land surfaces. To quantitatively assess the performances of PERSIANN-CCS, ERA5-Land, FY-4A, GSMaP, and IMERG, the five precipitation products were evaluated separately against CMPA data at daily scale over southern China during the study period (Figure 4a–e). In general, according to the validation results, both GSMaP and IMERG outperform the other three products (PERSIANN-CCS, ERA5-Land, and FY-4A), with the CC of 0.70 and 0.73 (0.48, 0.57, and 0.36) and BIAS of 21.95% and 21.41% (33.07%, 26.16%, and 52.14%), respectively. In terms of RMSE, the results of GSMaP are the lowest (11.81 mm/d) compared to those of PERSIANN-CCS, ERA5-Land, FY-4A, and IMERG for the entire summer of 2019.

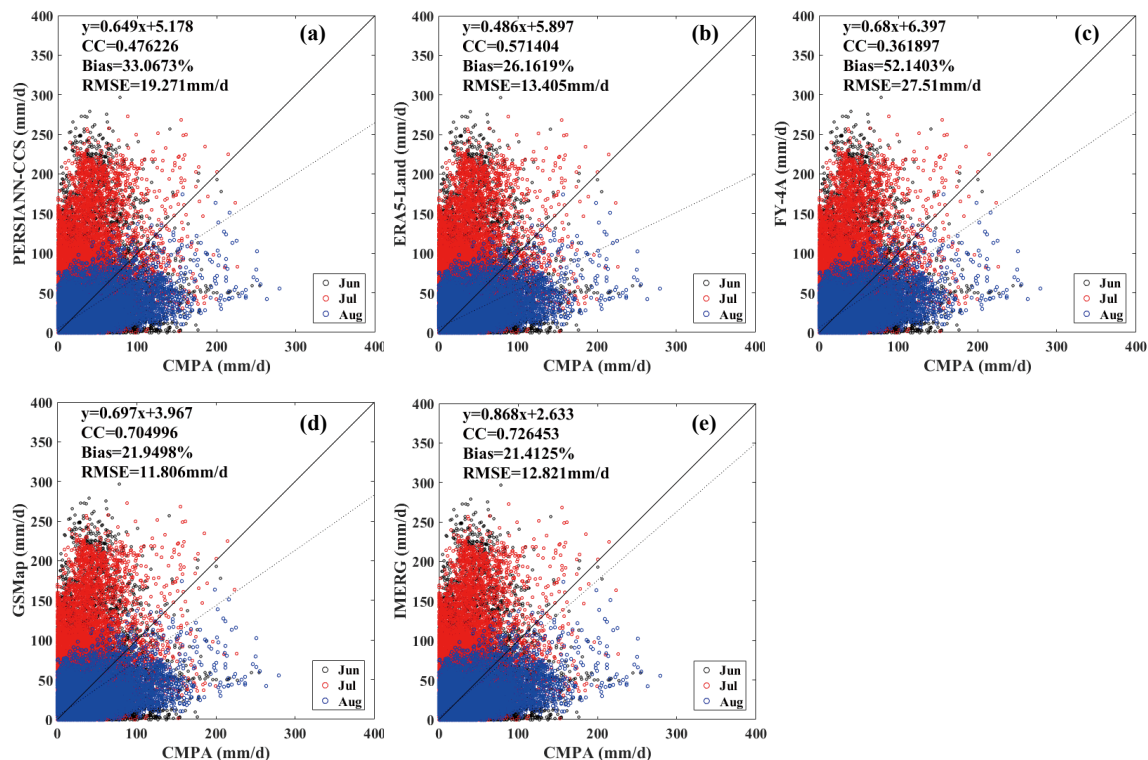


Figure 4. Validations of (a) PERSIANN-CCS, (b) ERA5-Land, (c) FY-4A, (d) GSMaP, and (e) IMERG at daily scale over southern China in summer 2019.

Table 4 presents the values of three indicators (CC, BIAS, and RMSE) of the five precipitation products at the daily scale in June, July, August, and the summer, respectively. The CC values of PERSIANN-CCS, ERA5-Land, GSMaP, and IMERG increase month by month and are obviously higher in August than those in July and June. FY-4A has the worst CC, BIAS, and RMSE values of all the precipitation products from June to August, except it has the lowest BIAS in June (13.51%). Additionally, the RMSE values of GSMaP are the lowest of all in summer, June, July, and August. The rankings of precipitation products most suitable for the study region are IMERG, GSMaP, ERA5-Land, PERSIANN-CCS, and FY-4A in summer, June, July, and August, respectively.

To demonstrate the regional error characteristics of precipitation datasets, we used Taylor diagrams focusing on precipitation intensity evaluation. As shown in Figure 5, the closer the points representing the satellite-based precipitation products are to the CMPA point marked by the black star, the better the accuracy. IMERG performs the best, with RMSD values of around 12.72, 13.65, 12.49, and 11.98 mm, and CC values of around 0.73, 0.70, 0.71, and 0.77 in June, July, August, and summer, respectively. GSMaP also shows the best performance, with the RMSD values of around 12.34, 11.28, 11.42, and 11.68 mm, and CC values of around 0.68, 0.68, 0.75, and 0.71 in June, July, August, and summer, respectively.

Meanwhile, FY-4A displays the largest values of RMSD and the lowest values of CC, meaning that it has the lowest similarity to CMPA in all four periods.

Table 4. Summaries of the results for PERSIANN-CCS, ERA5-Land, FY-4A, GSMaP, and IMERG at a daily scale over southern China in the summer of 2019.

Index	Dataset	June	July	August	Summer
CC	PERSIANN-CCS	0.45	0.53	0.61	0.48
	ERA5-Land	0.50	0.57	0.65	0.57
	FY-4A	0.44	0.45	0.42	0.43
	GSMaP	0.68	0.68	0.75	0.71
	IMERG	0.70	0.71	0.77	0.73
BIAS (%)	PERSIANN-CCS	28.38	89.14	−17.10	33.07
	ERA5-Land	33.93	28.30	15.68	26.16
	FY-4A	13.51	199.16	−51.01	52.14
	GSMaP	25.19	25.72	14.73	21.95
	IMERG	21.32	24.33	18.64	21.41
RMSE (mm/d)	PERSIANN-CCS	20.12	23.23	13.06	19.27
	ERA5-Land	15.31	11.91	12.82	13.40
	FY-4A	21.96	39.28	15.39	27.51
	GSMaP	12.51	11.43	11.47	11.81
	IMERG	13.77	12.61	12.06	12.82

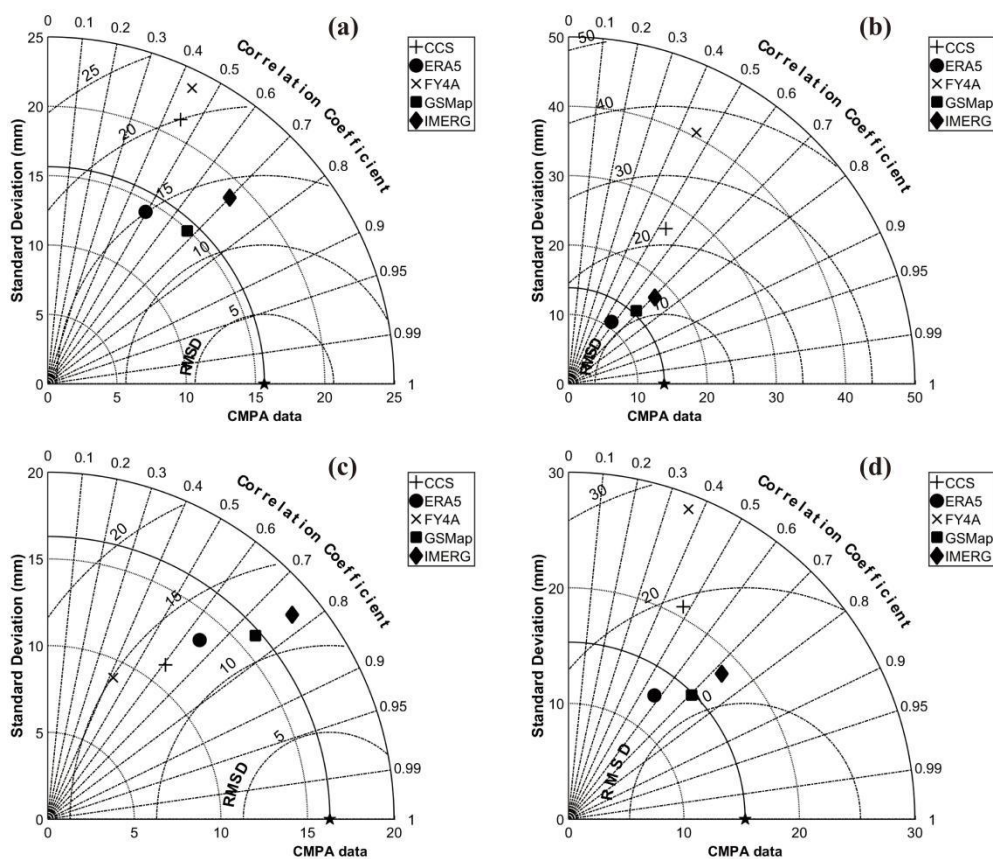


Figure 5. (a–d) Taylor diagrams of performances of PERSIANN-CCS, ERA5-Land, FY-4A, GSMaP, and IMERG against CMPA in terms of the centered root-mean-square difference, correlation coefficient, and standard deviation.

3.3. Hourly Scale Assessment of the Five Precipitation Products Based on Statistical Metrics

PERSIANN-CCS, ERA5-Land, FY-4A, GSMaP, and IMERG products were further compared at the hourly scale. Figures 6–11 illustrate the spatial patterns of CC, BIAS, RMSE, POD, FAR, and ETS of PERSIANN-CCS, ERA5-Land, FY-4A, GSMaP, and IMERG, respectively, against CMPA at an hourly scale and $0.1^\circ \times 0.1^\circ$ resolution over southern China in summer 2019. Overall, the spatial distributions of six classical indicators among different precipitation products are significantly different.

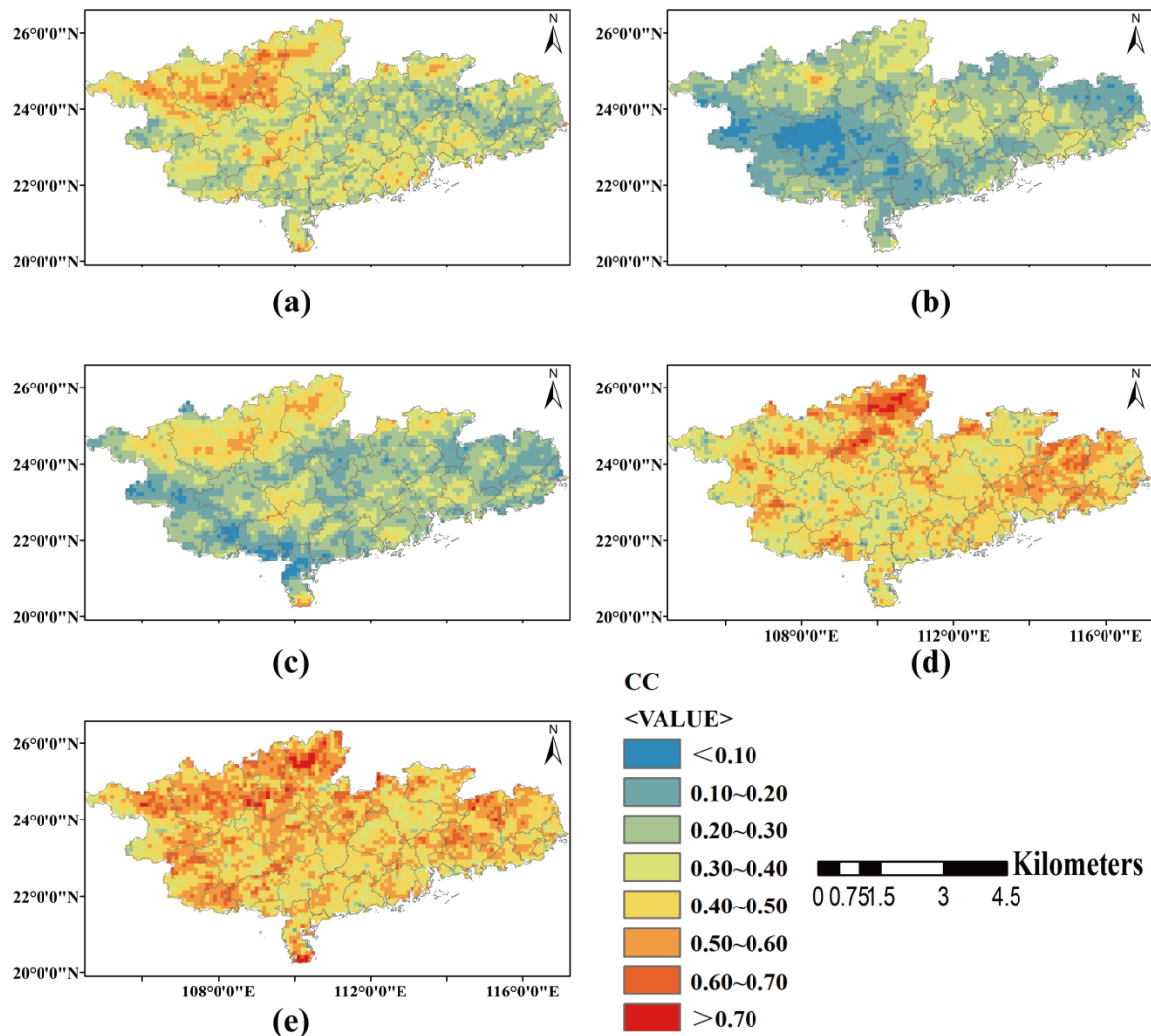


Figure 6. Spatial patterns in terms of correlation coefficient (CC) based on (a) PERSIANN-CCS, (b) ERA5-Land, (c) FY-4A, (d) GSMaP, and (e) IMERG against CMPA at hourly scale over southern China in summer 2019.

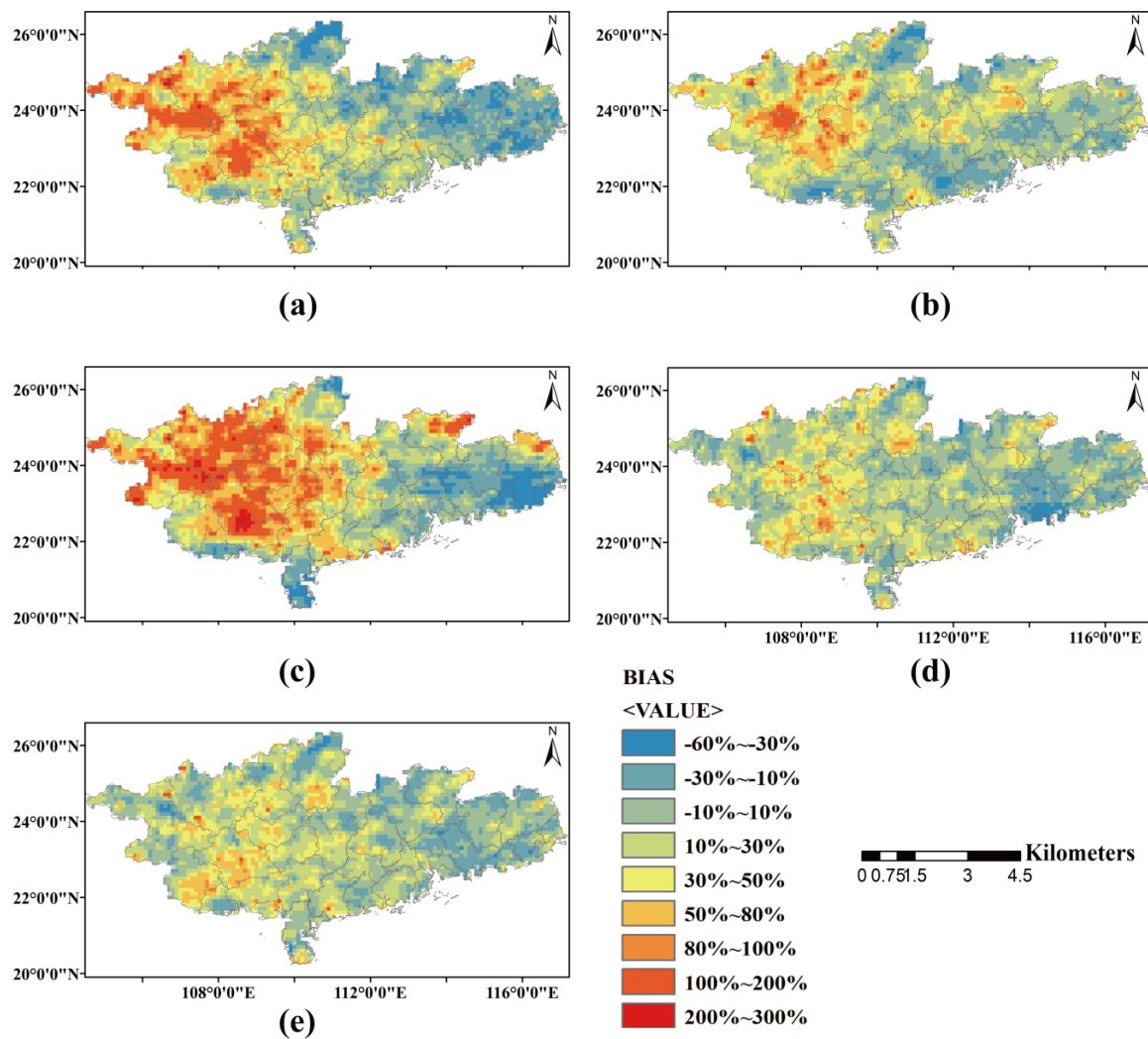


Figure 7. Spatial patterns in terms of relative bias (BIAS) based on (a) PERSIANN-CCS, (b) ERA5-Land, (c) FY-4A, (d) GSMaP, and (e) IMERG against CMPA at hourly scale over southern China in summer 2019.

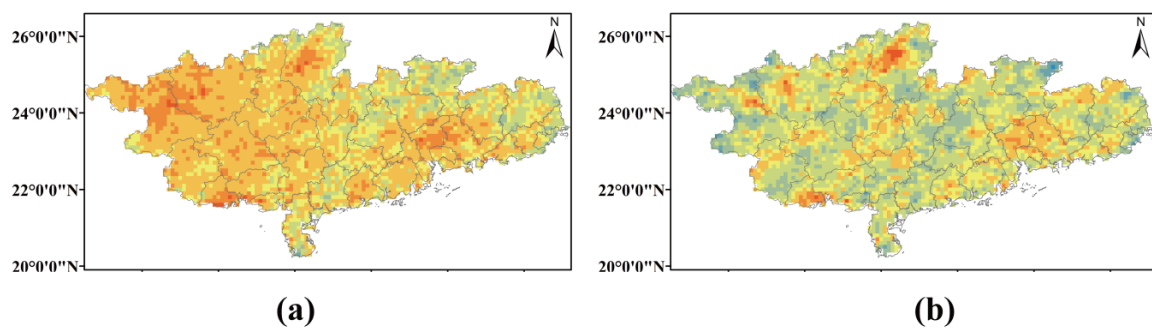


Figure 8. Cont.

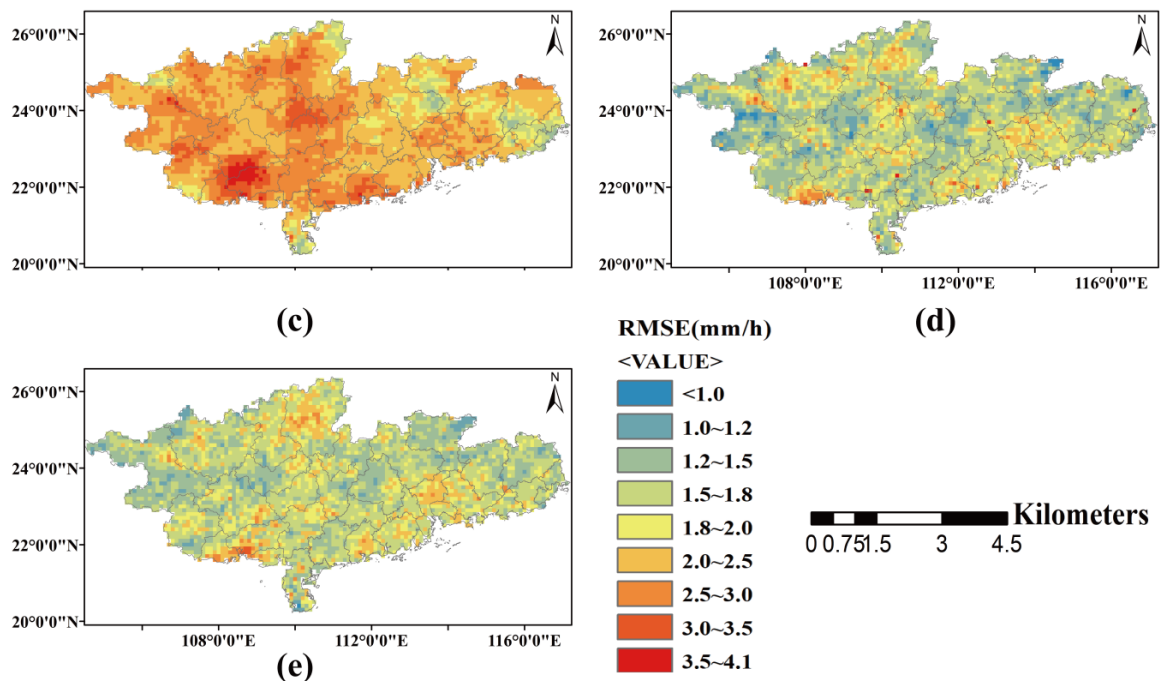


Figure 8. Spatial patterns in terms of root-mean-square error (RMSE) based on (a) PERSIANN-CCS, (b) ERA5-Land, (c) FY-4A, (d) GSMaP, and (e) IMERG against CMPA at hourly scale over southern China in summer 2019.

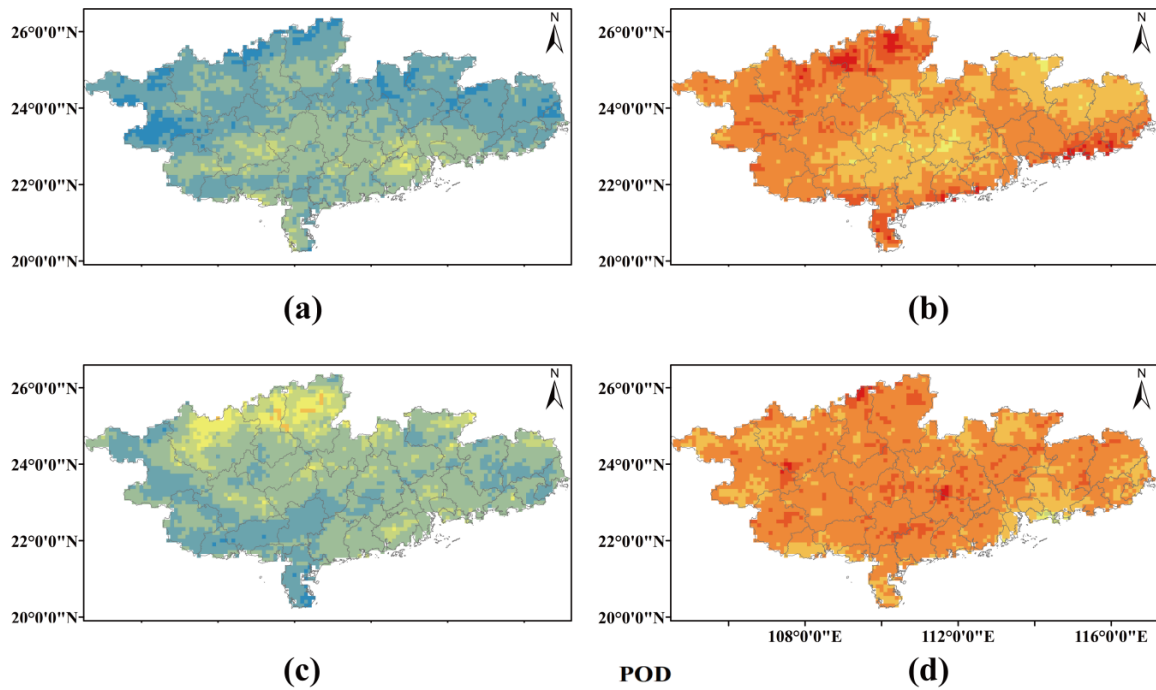


Figure 9. Cont.

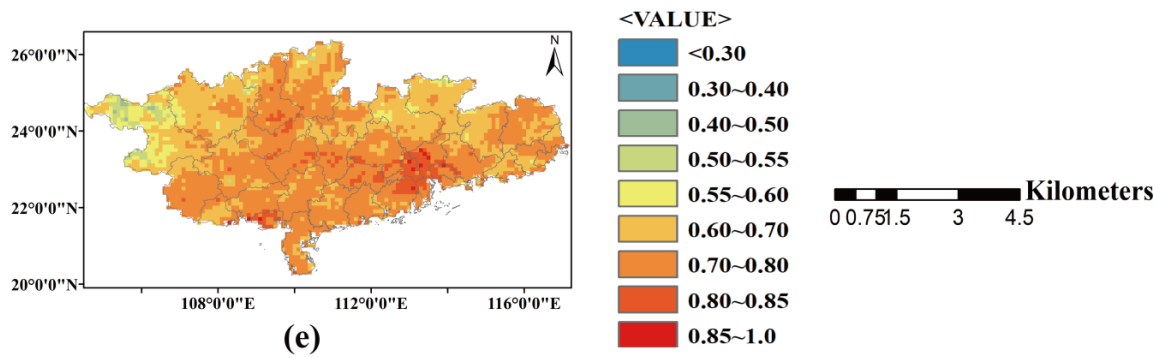


Figure 9. Spatial patterns in terms of probability of detection (POD) based on (a) PERSIANN-CCS, (b) ERA5-Land, (c) FY-4A, (d) GSMaP, and (e) IMERG against CMPA at hourly scale over southern China in summer 2019.

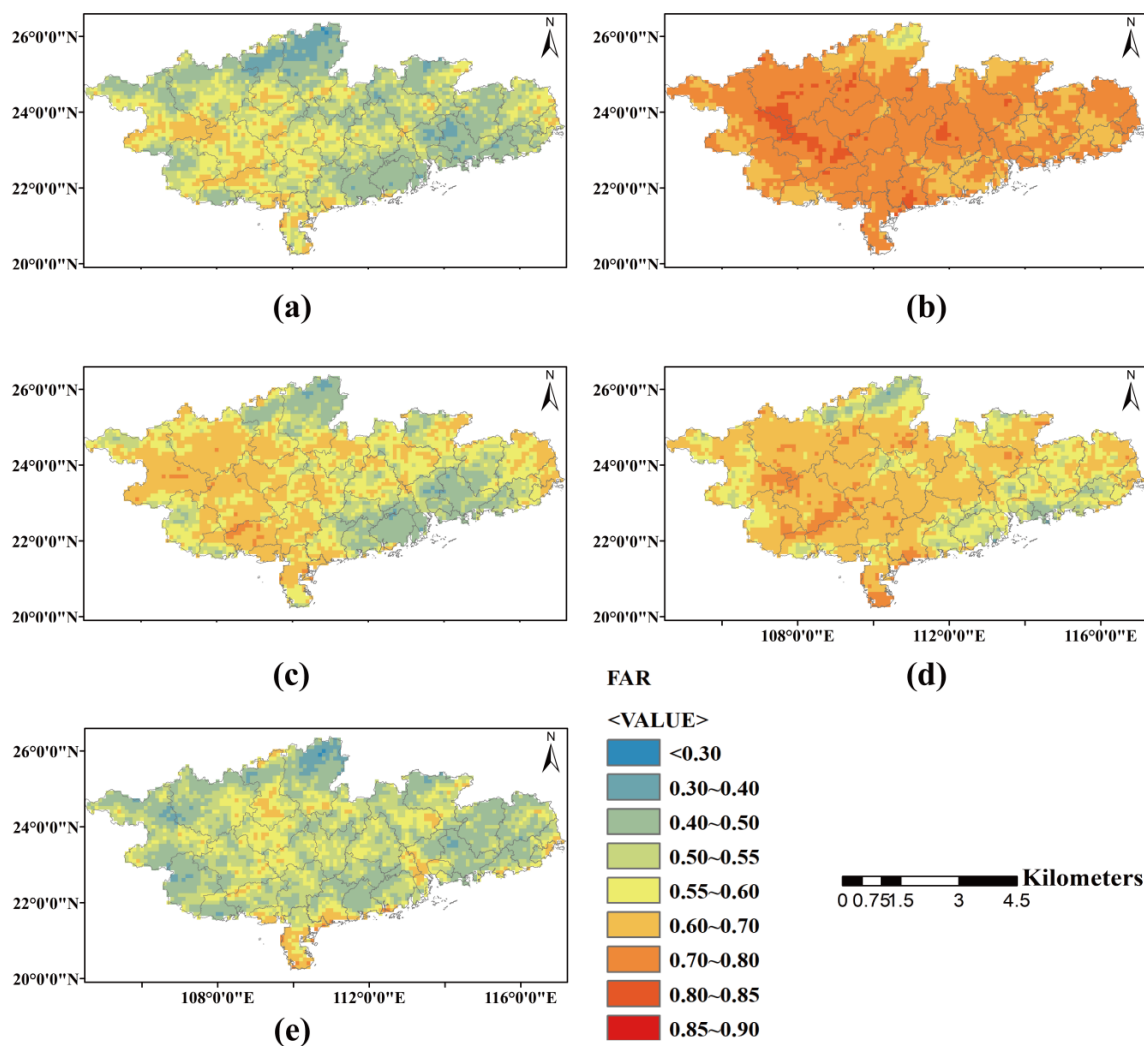


Figure 10. Spatial patterns in terms of false alarm ratio (FAR) based on (a) PERSIANN-CCS, (b) ERA5-Land, (c) FY-4A, (d) GSMaP, and (e) IMERG against CMPA at hourly scale over southern China in summer 2019.

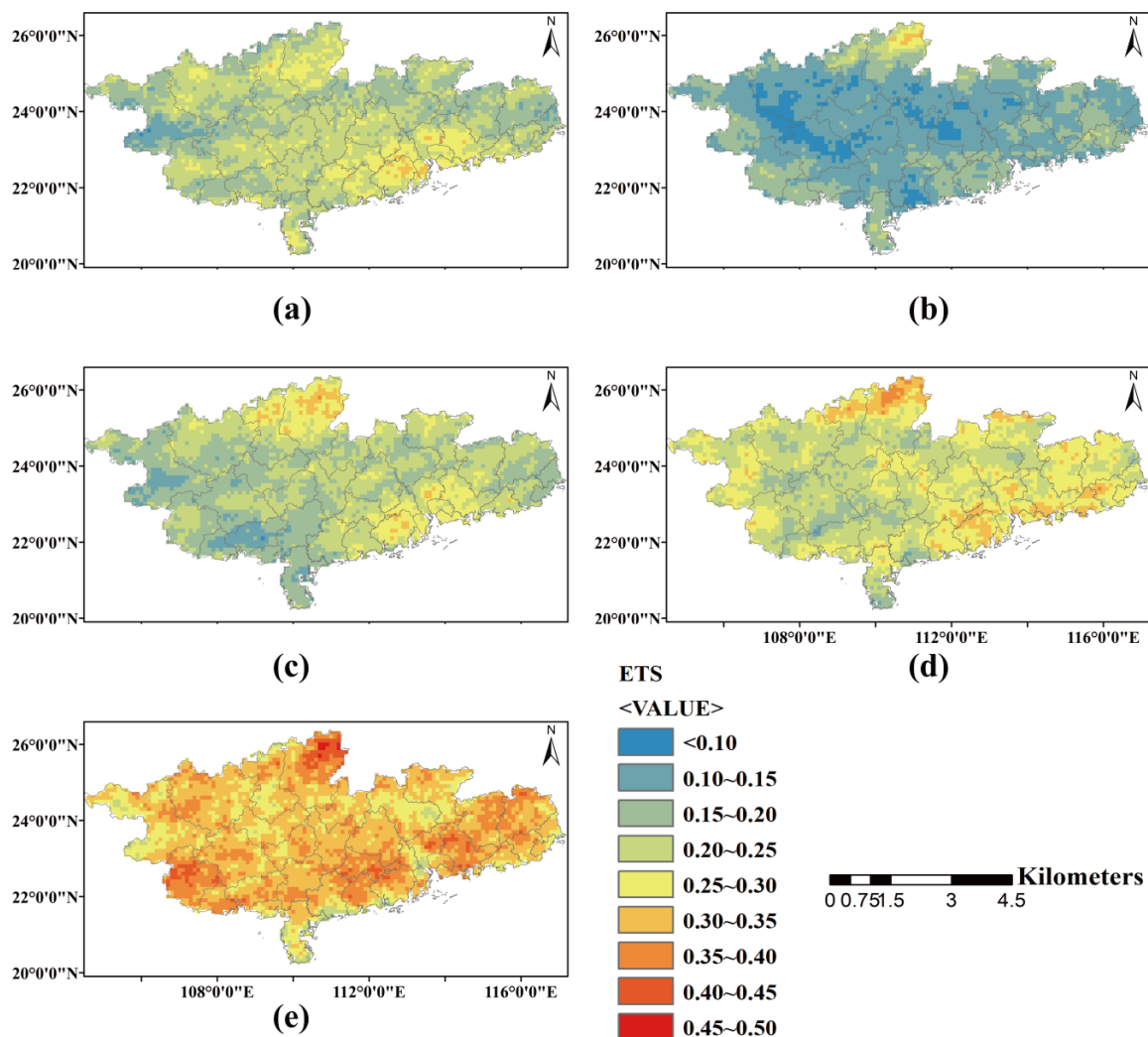


Figure 11. Spatial patterns in terms of equitable threat score (ETS) based on (a) PERSIANN-CCS, (b) ERA5-Land, (c) FY-4A, (d) GSMaP, and (e) IMERG against CMPA at hourly scale over southern China in summer 2019.

All the gridded precipitation products obtain better CCs in the northwest compared to other parts of the region (Figure 6a–e). The CC values of PERSIANN-CCS vary from 0 to 0.66 but are rarely larger than 0.6. FY-4A shows the smallest CC values, which are mainly below 0.5 and even less than 0.1 in some areas of the western and eastern regions. The CC values of ERA5-Land are slightly larger than FY-4A, especially in the west. GSMaP and IMERG share similar spatial patterns of CC, which are mainly above 0.4. Meanwhile, IMERG exhibits the best performance, with CC values larger than 0.5 or 0.7 in most of the region.

Based on the BIAS, the five satellite-based precipitation products obviously perform worse in the center of the western region (Figure 7a–e). The BIAS values of PERSIANN-CCS are larger than 30% over more than half of the region, whereas for the remaining area, it is below -30% , especially in the east. FY-4A is significantly overestimated and cannot capture the spatial characteristics of precipitation, with BIAS values worse than PERSIANN-CCS over southern China. ERA5-Land is slightly better than PERSIANN-CCS. IMERG and GSMaP share similar spatial patterns of BIAS and overestimate precipitation from an overall perspective, with BIAS values varying from -30% to 30% .

According to the RMSE (Figure 8a–e), FY-4A performs the worst in the whole region, especially in southwest areas with RMSE values larger than 3.5 mm/h. The RMSE values of PERSIANN-CCS are smaller than FY-4A but larger than ERA5-Land. Overall, IMERG and GSMaP perform better than the

other three precipitation products, and their differences in spatial distributions are small. Considering CC, BIAS, and RMSE statistics, IMERG might outperform other precipitation products, and FY-4A shows the worst performance.

As shown in Figure 9a–e, both the POD values of ERA5-Land and GSMaP are between 0.5 and 0.9 across the region, which are much better than those of PERSIANN-CCS and FY-4A (from around 0.2 to 0.6) and slightly better than IMERG (from around 0.4 to 0.9). Meanwhile, IMERG and GSMaP share similar distributions in estimating hourly precipitation occurrence and intensity, with especially high POD values in central areas. However, the FAR and ETS values of ERA5-Land are significantly worse (Figures 10b and 11b). Considering that ERA5-Land shows good performance at the daily scale in Table 4, the degradation of ERA5-Land at the hourly scale needs further investigation (Tang et al., 2020). In terms of FAR (Figure 10a–e), IMERG performs the best, follow by PERSIANN-CCS and FY-4A, respectively. GSMaP and ERA5-Land share similar spatial patterns of FAR, while they perform worse than the other three products. Regarding the spatial distributions of ETS (Figure 11a–e), IMERG shows the best performance, followed by the GSMaP. Considering the three contingency indices (POD, FAR, and ETS), IMERG also outperforms the other precipitation products.

Figure 12 illustrates the numerical distributions of six metrics (CC, BIAS, RMSE, POD, FAR, and ETS) for PERSIANN-CCS, ERA5-Land, FY-4A, GSMaP, and IMERG products over southern China. Averaged values of contingency indicators of the five products over 3652 grid pixels at hourly scale in summer 2019 are exhibited in Table 5. For IMERG, the metrics of CC, BIAS, RMSE, FAR, and ETS show better performance compared to the others, and GSMaP is close to IMERG among all products. In terms of the POD, ERA5-Land performs better than the satellite products IMERG, FY-4A, and PERSIANN-CCS, which is probably because ERA5-Land reanalysis precipitation products blend large amounts of data.

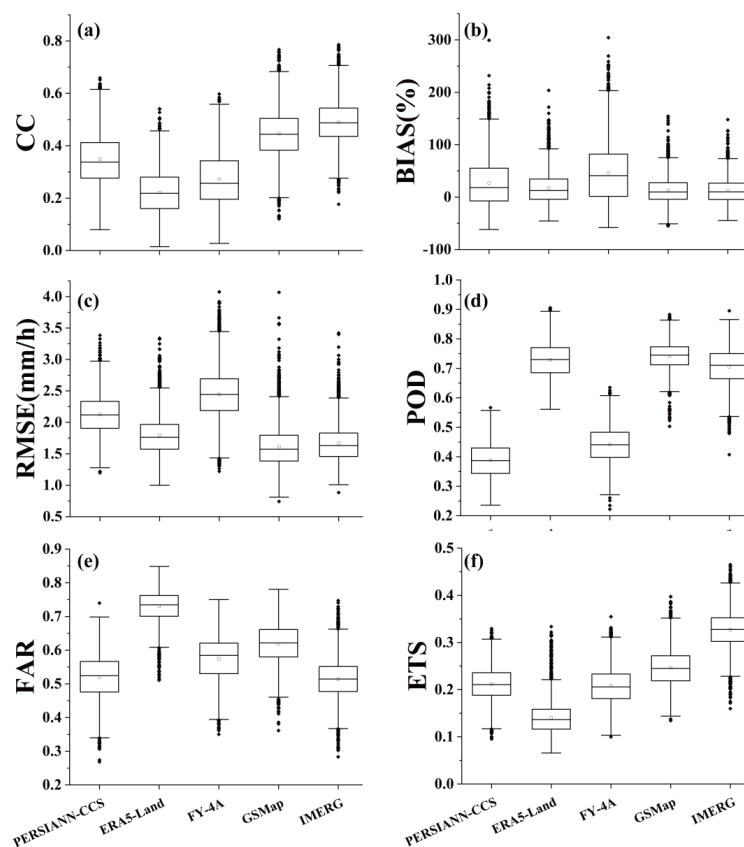


Figure 12. The numerical distributions of contingency statistics for PERSIANN-CCS, ERA5-Land, FY-4A, GSMaP, and IMERG in terms of (a) CC, (b) BIAS, (c) RMSE, (d) POD, (e) FAR, and (f) ETS, respectively.

Table 5. Averaged statistical indices for PERSIANN-CCS, ERA5-Land, FY-4A, GSMaP, and IMERG at hourly scale over southern China in summer 2019.

Index	PERSIANN-CCS	ERA5-Land	FY-4A	GSMaP	IMERG
CC	0.35	0.22	0.28	0.45	0.49
BIAS	27.67	18.26	48.41	13.00	12.49
RMSE	2.14	1.80	2.45	1.62	1.68
POD	0.39	0.73	0.45	0.74	0.70
FAR	0.52	0.73	0.57	0.62	0.51
ETS	0.21	0.14	0.21	0.25	0.33

4. Discussions

Five state-of-the-art satellites and reanalysis precipitation datasets were assessed using gridded in-situ rain gauge data in this study. Results provided insights into how different errors varied with precipitation intensities, elevation, and climate zones [19,37]. However, the spatiotemporal mismatch between the gauge data and satellite/reanalysis data could affect evaluation results [38]. One way to address the scale mismatch is to use them as hydrological model forcings and evaluate their performance against observed streamflow records [25,39]. Future studies should promote hydrological applications of the latest satellite-based QPEs at hourly and daily scales and continuously improve the IMERG and FY retrieval algorithms [23,40].

According to the results demonstrated above, we found that IMERG precipitation products showed good performance at both hourly and daily scales across the study region in summer 2019, followed by GSMaP. The gauge-corrected GSMaP and IMERG performed better than other QPEs in reducing various errors, especially the former, which had the largest POD [21]. In fact, the performances of PERSIANN-CCS, ERA5-Land, and FY-4A products were not satisfying. Our results were consistent with those detailed by Tang et al. [8] for spatial distribution. The differences between the algorithms and the corresponding correction technology may lead to different accuracy [41].

As shown in Table 1, benefiting from the short latency time (9 hours for FY-4A, 1 hour for PERSIANN-CCS, 2 months for ERA5-Land, 3 days for GSMaP, and 3.5 months for IMERG), FY-4A has more potential for use in real-time hydrological applications than IMERG [16,42–44]. Considering the shortcomings of the FY-4A in estimating heavy rainfall with large errors, the algorithm should be improved in the future to improve the monitoring ability for heavy rainfall so that the technique can be optimized for weather forecasting and flood warning [45].

5. Conclusions

Satellite-based precipitation products with fine quality and spatial-temporal resolutions play significant roles in forcing global climate, hydrological, and agricultural models, which are particularly useful over large and poorly gauged regions. To elucidate the strengths and weaknesses of recently released gridded precipitation datasets, we conducted a comprehensive evaluation of the performance of PERSIANN-CCS, ERA5-Land, FY-4A, GSMaP, and IMERG (0.1°/both daily and hourly), using rain-gauge data from CMPA as a reference, over southern China in summer 2019. The main conclusions of this study include:

- (1) All five products overestimate the accumulated rainfall in the summer of 2019, and FY-4A presents the most serious overestimation; additionally, FY-4A cannot capture the spatial and temporal distribution characteristics of precipitation over southern China.
- (2) IMERG and GSMaP perform better than PERSIANN-CCS, ERA5-Land, and FY-4A, both at daily and hourly time-scales, over southern China; IMERG correlates slightly better than GSMaP against CMPA data, while it performs worse than GSMaP in terms of POD.

- (3) The reanalysis product ERA5-Land performs better than PERSIANN-CCS and FY-4A at the daily scale but shows the worst CC, FAR, and ETS values of all precipitation products at the hourly scale.
- (4) The rankings of precipitation products most suitable for this region are IMERG, GSMaP, ERA5-Land, PERSIANN-CCS, and FY-4A at the daily scale; and IMERG, GSMaP, PERSIANN-CCS, FY-4A, and ERA5-Land at the hourly scale.

The comprehensive analysis of the quality of state-of-the-art gridded precipitation datasets presented in this study will provide valuable feedback for improving the current satellite-based precipitation retrieval algorithms as well as preliminary references for flood forecasting and natural disaster early warning. However, the updating of meteorological satellites is continually providing longer-range and more accurate FY products, and we only compare the FY-4A over southern China in summer 2019 in this work. In future work, we should evaluate the hydrological utility of the latest satellite-based QPEs. Further investigations should also be carried out to assess the underlying insights from IMERG retrieval algorithms for error and how errors propagate to hydrological simulations.

Author Contributions: Conceptualization, Z.G., X.C. and B.H.; methodology, Z.G. and Z.M.; analysis, Z.G.; writing—original draft preparation, Z.G.; writing—review and editing, Z.G., X.C., B.H., Z.M., J.Q. and D.L.; funding acquisition, Z.G., X.C. and B.H. All authors have read and agreed to the published version of the manuscript.

Funding: This research was funded by the National Key Research and Development Program of China (Grant No. 2016YFC0402603), National Natural Science Foundation of China (Grant No. U1911204, 51861125203, 91547202), China Postdoctoral Science Foundation (Grant No. 2019M662828) and the Consulting Research Project of Chinese Academy of Engineering (Grant No. 2019-ZD-34-01).

Acknowledgments: The authors' great gratitude is extended to the NSMC for providing FY-4A QPE. We also appreciate the extensive efforts of the developers of ground, satellite, and reanalysis precipitation datasets to make their products available.

Conflicts of Interest: The authors declare no conflict of interest.

References

1. Sharifi, E.; Eitzinger, J.; Dorigo, W.A. Performance of the State-Of-The-Art Gridded Precipitation Products over Mountainous Terrain: A Regional Study over Austria. *Remote Sens.* **2019**, *11*, 2018. [[CrossRef](#)]
2. Beck, H.E.; Wood, E.F.; Pan, M.; Fisher, C.K.; Miralles, D.G.; Van Dijk, A.I.J.M.; McVicar, T.R.; Adler, R.F. MSWEP V2 Global 3-Hourly 0.1° Precipitation: Methodology and Quantitative Assessment. *Bull. Am. Meteorol. Soc.* **2019**, *100*, 473–500. [[CrossRef](#)]
3. Ma, Z.; Xu, J.; He, K.; Han, X.; Ji, Q.; Wang, T.; Xiong, W.; Hong, Y. An updated moving window algorithm for hourly-scale satellite precipitation downscaling: A case study in the Southeast Coast of China. *J. Hydrol.* **2020**, *581*, 124378. [[CrossRef](#)]
4. Ren, L.; Wang, B.; Shi, C.; Cui, W.; Zhao, C.; Liu, Y.; Ren, L.; Zhang, L.; Zhu, Y.; Chen, T.; et al. Evaluation of hydrological utility of IMERG Final run V05 and TMPA 3B42V7 satellite precipitation products in the Yellow River source region, China. *J. Hydrol.* **2018**, *567*, 696–711. [[CrossRef](#)]
5. Gao, Z.; Long, D.; Tang, G.; Zeng, C.; Huang, J.; Hong, Y. Assessing the potential of satellite-based precipitation estimates for flood frequency analysis in ungauged or poorly gauged tributaries of China's Yangtze River basin. *J. Hydrol.* **2017**, *550*, 478–496. [[CrossRef](#)]
6. Xue, X.; Hong, Y.; Limaye, A.S.; Gourley, J.J.; Huffman, G.J.; Khan, S.I.; Dorji, C.; Chen, S. Statistical and hydrological evaluation of TRMM-based Multisatellite precipitation analysis over the wangchu basin of bhutan: Are the latest satellite precipitation products 3B42V7 ready for use in ungauged basins? *J. Hydrol.* **2013**, *449*, 91–99. [[CrossRef](#)]
7. Gebregiorgis, A.S.; Hossain, F. Understanding the Dependence of Satellite Rainfall Uncertainty on Topography and Climate for Hydrologic Model Simulation. *IEEE Trans. Geosci. Remote Sens.* **2013**, *51*, 704–718. [[CrossRef](#)]
8. Tang, G.; Clark, M.P.; Papalexiou, S.; Ma, Z.; Hong, Y. Have satellite precipitation products improved over last two decades? A comprehensive comparison of GPM IMERG with nine satellite and reanalysis datasets. *Remote Sens. Environ.* **2020**, *240*, 111697. [[CrossRef](#)]

9. Huffman, G.J.; Adler, R.F.; Bolvin, D.T.; Nelkin, E.J. The TRMM multi-satellite precipitation analysis (TMPA). In *Satellite Rainfall Applications for Surface Hydrology*; Springer: Dordrecht, The Netherlands, 2010; pp. 3–22.
10. Huffman, G.J.; Bolvin, D.T.; Braithwaite, D.; Hsu, K.; Joyce, R.; Kidd, C.; Nelkin, E.J.; Sorooshian, S.; Tan, J.; Xie, P. NASA Global Precipitation Measurement (GPM) Integrated Multi-satellite Retrievals for GPM (IMERG). In *Algorithm Theoretical Basis Document (ATBD)*; NASA/GSFC: Greenbelt, MD, USA, 2019.
11. Joyce, R.J.; Janowiak, J.E.; Arkin, P.A.; Xie, P. CMORPH: A Method that Produces Global Precipitation Estimates from Passive Microwave and Infrared Data at High Spatial and Temporal Resolution. *J. Hydrometeorol.* **2004**, *5*, 287–296. [[CrossRef](#)]
12. Hong, Y.; Gochis, D.; Cheng, J.-T.; Hsu, K.-L.; Sorooshian, S. Evaluation of PERSIANN-CCS Rainfall Measurement Using the NAME Event Rain Gauge Network. *J. Hydrometeorol.* **2007**, *8*, 469–482. [[CrossRef](#)]
13. Nguyen, P.; Ombadi, M.; Sorooshian, S.; Hsu, K.-L.; AghaKouchak, A.; Braithwaite, D.; Ashouri, H.; Thorstensen, A.R. The PERSIANN family of global satellite precipitation data: A review and evaluation of products. *Hydrol. Earth Syst. Sci.* **2018**, *22*, 5801–5816. [[CrossRef](#)]
14. Mega, T.; Ushio, T.; Takahiro, M.; Kubota, T.; Kachi, M.; Oki, R. Gauge-Adjusted Global Satellite Mapping of Precipitation. *IEEE Trans. Geosci. Remote Sens.* **2018**, *57*, 1928–1935. [[CrossRef](#)]
15. Beck, H.E.; Van Dijk, A.I.J.M.; Levizzani, A.F.V.; Schellekens, J.; Miralles, D.G.; Martens, B.; De Roo, A. MSWEP: 3-hourly 0.25° global gridded precipitation (1979–2015) by merging gauge, satellite, and reanalysis data. *Hydrol. Earth Syst. Sci.* **2017**, *21*, 589–615. [[CrossRef](#)]
16. Xu, J.; Ma, Z.; Tang, G.; Ji, Q.; Min, X.; Wan, W.; Shi, Z. Quantitative Evaluations and Error Source Analysis of Fengyun-2-Based and GPM-Based Precipitation Products over Mainland China in Summer, 2018. *Remote Sens.* **2019**, *11*, 2992. [[CrossRef](#)]
17. Vitolo, C.; Di Giuseppe, F.; Barnard, C.; Coughlan, R.; San-Miguel-Ayanz, J.; Libertá, G.; Krzeminski, B. ERA5-based global meteorological wildfire danger maps. *Sci. Data* **2020**, *7*, 1–11. [[CrossRef](#)]
18. Yu, C.; Hu, D.; Liu, M.; Wang, S.; Di, Y. Spatio-temporal accuracy evaluation of three high-resolution satellite precipitation products in China area. *Atmos. Res.* **2020**, *241*, 104952. [[CrossRef](#)]
19. Sun, Q.; Miao, C.; Duan, Q.; Ashouri, H.; Sorooshian, S.; Hsu, K.L. A Review of Global Precipitation Data Sets: Data Sources, Estimation, and Intercomparisons. *Rev. Geophys.* **2018**, *56*, 79–107. [[CrossRef](#)]
20. Hong, Y.; Tang, G.; Ma, Y.; Huang, Q.; Han, Z.; Zeng, Z.; Yang, Y.; Wang, C.; Guo, X. *Remote Sensing Precipitation: Sensors, Retrievals, Validations, and Applications*; Observation and Measurement Ecohydrology; Springer: Berlin/Heidelberg, Germany, 2018.
21. Lu, D.; Young, B. Evaluation and Hydrological Utility of the Latest GPM IMERG V5 and GSMaP V7 Precipitation Products over the Tibetan Plateau. *Remote Sens.* **2018**, *10*, 2022. [[CrossRef](#)]
22. Mohammed, I.N.; Bolten, J.D.; Srinivasan, R.; Lakshmi, V. Improved Hydrological Decision Support System for the Lower Mekong River Basin Using Satellite-Based Earth Observations. *Remote Sens.* **2018**, *10*, 885. [[CrossRef](#)]
23. Jiang, L.; Bauer-Gottwein, P. How do GPM IMERG precipitation estimates perform as hydrological model forcing? Evaluation for 300 catchments across Mainland China. *J. Hydrol.* **2019**, *572*, 486–500. [[CrossRef](#)]
24. Shao, J.; Gao, H.; Wang, X.; Zhang, Q. Application of Fengyun-4 Satellite to Flood Disaster Monitoring through a Rapid Multi-Temporal Synthesis Approach. *J. Meteorol. Res.* **2020**, *34*, 720–731. [[CrossRef](#)]
25. Maggioni, D.; Massari, C. On the performance of satellite precipitation products in riverine flood modeling: A review. *J. Hydrol.* **2018**, *558*, 214–224. [[CrossRef](#)]
26. Tang, G.; Long, D.; Hong, Y.; Gao, J.; Wan, W. Documentation of multifactorial relationships between precipitation and topography of the Tibetan Plateau using spaceborne precipitation radars. *Remote Sens. Environ.* **2018**, *208*, 82–96. [[CrossRef](#)]
27. Wang, T.; Tang, G. Spatial Variability and Linkage between Extreme Convections and Extreme Precipitation Revealed by 22-Year Space-Borne Precipitation Radar Data. *Geophys. Res. Lett.* **2020**, *47*, 088437. [[CrossRef](#)]
28. Vizi, E.K.; Cook, K.H. Observed relationship between the Turkana low-level jet and boreal summer convection. *Clim. Dyn.* **2019**, *53*, 4037–4058. [[CrossRef](#)]
29. Zhang, A.; Xiao, L.; Min, C.; Chen, S.; Kulie, M.; Huang, C.; Liang, Z. Evaluation of latest GPM-Era high-resolution satellite precipitation products during the May 2017 Guangdong extreme rainfall event. *Atmos. Res.* **2019**, *216*, 76–85. [[CrossRef](#)]
30. Islam, A.; Yu, B.; Cartwright, N. Assessment and comparison of five satellite precipitation products in Australia. *J. Hydrol.* **2020**, *590*, 125474. [[CrossRef](#)]

31. Zhou, Z.; Guo, B.; Xing, W.; Zhou, J.; Xu, F.; Xu, Y. Comprehensive evaluation of latest GPM era IMERG and GSMaP precipitation products over mainland China. *Atmos. Res.* **2020**, *246*, 105132. [[CrossRef](#)]
32. Li, X.; Chen, Y.; Wang, H.; Zhang, Y. Assessment of GPM IMERG and radar quantitative precipitation estimation (QPE) products using dense rain gauge observations in the Guangdong-Hong Kong-Macao Greater Bay Area, China. *Atmos. Res.* **2020**, *236*, 104834. [[CrossRef](#)]
33. Shen, Y.; Zhao, P.; Pan, Y.; Yu, J. A high spatiotemporal gauge-satellite merged precipitation analysis over China. *J. Geophys. Res. Atmos.* **2014**, *119*, 3063–3075. [[CrossRef](#)]
34. Yong, B.; Ren, L.-L.; Hong, Y.; Wang, J.-H.; Yong, B.; Jiang, S.; Chen, X.; Wang, W. Hydrologic evaluation of Multisatellite Precipitation Analysis standard precipitation products in basins beyond its inclined latitude band: A case study in Laohahe basin, China. *Water Resour. Res.* **2010**, *46*, 759–768. [[CrossRef](#)]
35. Copernicus Climate Change Service (C3S). ERA5: Fifth Generation of ECMWF Atmospheric Reanalyses of the Global Climate. Copernicus Climate Change Service Climate Data Store (CDS): July 2019. Available online: <https://cds.climate.copernicus.eu/cdsapp#!/home> (accessed on 23 October 2020).
36. Taylor, K.E. Summarizing multiple aspects of model performance in a single diagram. *J. Geophys. Res. Atmos.* **2001**, *106*, 7183–7192. [[CrossRef](#)]
37. Xu, X.; Frey, S.K.; Boluwade, A.; Erler, A.R.; Khader, O.; Lapen, D.R.; Sudicky, E. Evaluation of variability among different precipitation products in the Northern Great Plains. *J. Hydrol. Reg. Stud.* **2019**, *24*, 100608. [[CrossRef](#)]
38. Tang, G.; Behrangi, A.; Long, D.; Li, C.; Hong, Y. Accounting for spatiotemporal errors of gauges: A critical step to evaluate gridded precipitation products. *J. Hydrol.* **2018**, *559*, 294–306. [[CrossRef](#)]
39. Zhang, D.; Liu, X.; Bai, P.; Li, X. Suitability of Satellite-Based Precipitation Products for Water Balance Simulations Using Multiple Observations in a Humid Catchment. *Remote Sens.* **2019**, *11*, 151. [[CrossRef](#)]
40. Chen, Y.; Yu, Z.; Han, W.; He, J.; Chen, M. Case Study of a Retrieval Method of 3D Proxy Reflectivity from FY-4A Lightning Data and Its Impact on the Assimilation and Forecasting for Severe Rainfall Storms. *Remote Sens.* **2020**, *12*, 1165. [[CrossRef](#)]
41. Sunilkumar, K.; Narayana, R.T.; Saikranthi, K.; Purnachandra, M.R. Comprehensive evaluation of multisatellite precipitation estimates over India using gridded rainfall data. *J. Geophys. Res. Atmos.* **2015**, *120*, 8987–9005. [[CrossRef](#)]
42. Mastrantonas, N.; Bhattacharya, B.; Shibuo, Y.; Rasmy, M.; Espinoza-Dávalos, G.; Solomatine, D. Evaluating the Benefits of Merging Near-Real-Time Satellite Precipitation Products: A Case Study in the Kinu Basin Region, Japan. *J. Hydrometeorol.* **2019**, *20*, 1213–1233. [[CrossRef](#)]
43. Massari, C.; Brocca, L.; Pellarin, T.; Abramowitz, G.; Filippucci, P.; Ciabatta, L.; Maggioni, V.; Kerr, Y.; Prieto, D.F. A daily 25 km short-latency rainfall product for data-scarce regions based on the integration of the Global Precipitation Measurement mission rainfall and multiple-satellite soil moisture products. *Hydrol. Earth Syst. Sci.* **2020**, *24*, 2687–2710. [[CrossRef](#)]
44. Qingping, W.; Xiaojing, W.; Yangquan, C.; Jie, D. Visualization and Application of FY-4A Satellite Data. *Meteorol. Ence Technol.* **2019**, *3*, 502–507.
45. Li, S.; Yue, J.; Wang, X.; Li, C.; Liu, H.; Li, G. Precipitation Characteristics of an Abrupt Heavy Rainfall Event over the Complex Terrain of Southwest China Observed by the FY-4A Satellite and Doppler Weather Radar. *Water* **2020**, *12*, 2502. [[CrossRef](#)]

Publisher’s Note: MDPI stays neutral with regard to jurisdictional claims in published maps and institutional affiliations.



© 2020 by the authors. Licensee MDPI, Basel, Switzerland. This article is an open access article distributed under the terms and conditions of the Creative Commons Attribution (CC BY) license (<http://creativecommons.org/licenses/by/4.0/>).